

EXPLOITATION OF MOF DECOMPOSITION MECHANISMS TO TAILOR MOF-DERIVED CARBON STRUCTURE IN MONO- AND MULTIMETALLIC PCN-250

Joshua A. Powell¹, Hengyu Lin¹, Yu-Chuan Hsu¹, Desirée E. Young², and Hong-Cai Zhou^{1*}

¹ Department of Chemistry, Texas A&M University, College Station TX 77843

² *framergy*, Inc., College Station TX 77845

Abstract

Metal-organic framework (MOF)-templated materials, such as MOF-derived carbons (MOF_dCs), are attractive materials for applications such as electrocatalysis and energy storage. Unfortunately, the black-box nature of their synthesis remains a barrier to their implementation, as it is difficult to target specific structural features or properties in the final material. In this work, we use the well-established decomposition mechanism of the iron-MOF PCN-250 to design a two-step MOF calcination procedure that produces a MOF_dC exhibiting both high porosity and monophasic iron(II,III) oxide. We further apply this procedure to bimetallic PCN-250 to form mixed-metal oxides with an iron(II,III) oxide-type structure. While the procedure successfully produced the target structure for cobalt- and manganese-doped PCN-250, it was unsuccessful for the nickel-doped PCN-250 due to the increased corrosion-resistance of the iron-nickel alloy intermediate.

Introduction

Metal-organic frameworks (MOFs) are a promising material for a wide array of applications due to their structural versatility and high porosity. Despite this promise, few MOFs have been applied commercially, in large part due to their poor stability.¹⁻³ As such, researchers have turned to using MOFs as templates for alternative materials, such as MOF-derived carbons (MOFDCs), that retain the high porosity and structural versatility of MOFs, but with significantly improved thermal and chemical stability.⁴⁻⁶ MOFDCs are comprised of a porous carbon matrix derived from the organic linkers of the MOF, often with nanoparticulate metal species derived from the inorganic building units (IBUs) of the MOF embedded throughout the carbon. A wide array of MOFs have been calcined to form MOFDCs, with early work emphasizing the calcination of zinc-based MOFs due to the ease of removing the zinc ions through evaporation and an interest in the development of highly-structured microporous carbon.^{4, 7} More recent studies have begun to explore the benefits of metal-containing MOFDCs, as the MOF-templated synthesis strategy tends to produce more highly dispersed metal or metal oxide species than traditional synthetic methods used to generate nanoparticle@porous carbon materials, such as wet impregnation.⁸⁻¹¹

Of particular interest is the development of MOFDCs containing bimetallic iron oxide nanoparticles, as bimetallic iron oxides hold great promise as catalysts for a variety of electrocatalytic and industrial applications.¹²⁻¹⁴ Specifically, the iron(II,III) oxide structure is desirable for catalysis, as it is more active than iron(III) oxide and more stable than iron(II) oxide.^{15, 16} Doping elements such as nickel or cobalt into the

structure significantly increases the activity of iron(II,III) oxide towards water splitting and nitrate reduction reactions.^{12, 13} Furthermore, incorporation of iron(II,III) oxide nanoparticles into a porous carbon matrix provides both a conductive substrate and a high concentration of readily accessible active sites due to the porosity. Fortunately, iron MOFs are relatively easy to synthesize and can be readily doped with heterometals to form bimetallic MOF structures.¹⁷⁻²⁰ Upon calcination, the multimetallic clusters often form alloys or other mixed-metal phases wherein both metals are incorporated in a single lattice structure,²¹⁻²⁴ however precise control over the phase is not always possible. The templating effect of the MOF structure can also provide avenues for synthesizing bimetallic species that are otherwise unobtainable via traditional inorganic synthetic methods.²⁵

A recent study by the Zhou group investigated the dependence of MOF_dC structure on the calcination conditions for an iron-based MOF, PCN-250 (PCN = porous coordination network).¹⁰ When the MOF was calcined in an oxidizing atmosphere, such as air or carbon dioxide, the resulting MOF_dC exhibited low porosity, as combustion of the linkers led to premature framework collapse. In contrast, calcination in a non-oxidizing atmosphere produced a carbon matrix with higher porosity that bore a greater resemblance to the template framework. On the other hand, calcination in non-oxidizing atmospheres provided poor phase control over the nanoparticulate iron species, as the iron(0) nanoparticles produced via oxidative decarboxylation of the decomposing linker were vigorously oxidized to a mixture of iron(II,III) and iron(III) oxides upon exposure to ambient air, while calcination in the gently oxidizing atmosphere of carbon dioxide

produced only the iron(II,III) oxide phase, as the iron(0) was gently oxidized throughout the calcination process.^{10, 26, 27} While the reported calcination strategies utilizing a single gas were unable to produce a MOF_dC containing both high porosity and a single iron(II,III) oxide phase, the Zhou group described the decomposition mechanism of PCN-250 in detail.¹⁰ Additionally, the Chapman group has studied the decomposition of multimetallic PCN-250-Fe₂M (M = Co, Ni) at lower temperatures in a reducing gas environment.²⁸ They found that the heterometals were not well-incorporated into the structure of the iron oxide nanoparticles that were produced from the clusters, instead forming distinct metallic nanoparticles that, in the case of cobalt, were alloyed with iron not incorporated in the iron oxide structure. They also reported that nickel ions were extracted from the IBU prior to the decomposition of the MOF, further encouraging phase separation of the two metals.²⁸

In light of this mechanistic understanding, we set out to develop a method that would both maximize the porosity of the MOF_dC and produce only the iron(II,III) oxide phase of iron oxide. Furthermore, we wanted to determine the generalizability of the procedure to control the formation of mixed-metal oxides with an iron(II,III) oxide structure from multimetallic PCN-250.

Experimental

Synthesis of PCN-250-Fe₂M (M = Mn, Co, Ni)

PCN-250-Fe₂M was synthesized according to the literature.¹⁷ Iron(III) nitrate nonahydrate (8 g) and metal(II) nitrate (M = Mn, Co, Ni, 5 eq) were dissolved in water

(70 mL). Separately, sodium acetate trihydrate (42 g) was dissolved in 70 mL of water and added to the metal nitrate solution while stirring. The brown precipitate (Fe_2M cluster) was collected by vacuum filtration and washed with water and ethanol.

A solution of 3,3',5,5'-azobenzene tetracarboxylic acid (H_4ABTC , 1 g), Fe_2M cluster (1 g) and acetic acid (100 mL) in dimethylformamide (DMF, 200 mL) was sonicated in a 500 mL Schott bottle. The solution was heated in an oven at 140 °C for 12 h. After cooling to room temperature, the dark brown crystals were collected by vacuum filtration and washed with DMF and methanol. The MOF was dried at 80 °C overnight. Additional characterization data of the MOFs can be found in the Supplemental Information.

Calcination of PCN-250- Fe_2M ($M = \text{Mn}, \text{Fe}, \text{Co}, \text{Ni}$)

Approximately 300 mg of template MOF was spread over the bottom of an alumina boat and placed in a tube furnace. The tube was flushed with nitrogen for 20 minutes, then the sample was heated to 500 °C for 4 hours under a flow of nitrogen gas (100 mL/min). The sample was then heated for a further 2 hours under a flow of carbon dioxide gas (100 mL/min). The sample was cooled to room temperature and collected. Additional single-step calcinations were performed where the sample was cooled and exposed to ambient air without heating in carbon dioxide.

CAUTION! A nanoparticulate $\text{Fe}(0)$ species is formed when PCN-250 is calcined in a non-oxidizing atmosphere. This species may spontaneously oxidize in a highly exothermic reaction upon exposure to air. To ensure complete oxidation by carbon dioxide, the sample should be spread thinly along the bottom of the boat. Samples should

be transferred directly to a glass or alumina container following synthesis in case of incomplete oxidation.

Results and Discussion

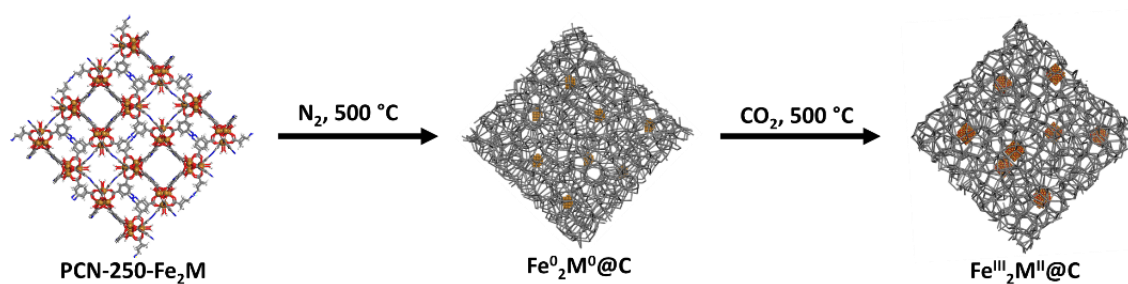
PCN-250-Fe₃

Previous studies of the decomposition and carbonization mechanisms of PCN-250-Fe₃ have shown that highly porous MOF_dCs are best obtained by carbonizations in the presence of non-oxidizing gases such as nitrogen or argon.¹⁰ However, the iron(II,III) oxide phase cannot be selectively formed in the presence of these non-oxidizing gases, as the oxidative decomposition of the linker reduces the iron of the cluster to iron(0). When a non-oxidizing calcination environment is used, the iron remains in the 0 oxidation state until it is exposed to ambient air when the synthesis is complete, at which point it is oxidized to a mixture of iron(II,III) and iron(III) oxides. In contrast, calcination of the MOF in a slightly oxidizing atmosphere, such as carbon dioxide, produces only an iron(II,III) oxide phase, however the resulting MOF_dC is significantly less porous due to premature framework collapse and partial combustion of the carbon matrix.¹⁰

Therefore, we designed a two-step calcination process to both maximize porosity and selectively form the iron(II,III) oxide phase (Scheme 2). In the first step, the MOF was calcined under a flow of nitrogen gas to carbonize the organic components of the MOF with minimal framework collapse or combustion. By limiting combustion of the organic linkers, the framework and pore structure of the MOF are better maintained to

produce a highly porous carbon matrix. As a consequence of the oxidative decarboxylation of the linkers, the iron-oxo clusters are reduced to iron(0) nanoparticles that are not air stable.^{10, 26, 27} Once the framework is completely carbonized, the material was further calcined under a flow of carbon dioxide gas, which is gently oxidizing under the elevated temperature conditions.²⁹ This step results in gentle oxidation of the iron(0) nanoparticles to produce iron(II,III) oxide and limits overoxidation to iron(III) oxide.

Scheme 1. Two-step calcination procedure for PCN-250-Fe₂M (M = Mn, Fe, Co, Ni).



Powder X-ray diffraction (PXRD) of the MOF_dC confirms that no residual MOF structure remains in the final MOF_dC, as evidenced by the absence of peaks in the low angle region (Figure 1a). Furthermore, only an iron(II,III) oxide phase is present in the final material, with no evidence of iron(III) oxide or iron(0). This determination is further supported by X-ray photoelectron spectroscopy (XPS) experiments, which show that the binding energy of the iron agrees well with the literature for iron(II,III) oxide (Figure 1c). The average size of the iron(II,III) oxide nanoparticles is 8.1 nm as determined by Rietveld refinement of the powder pattern (see Supplemental Information for details). In contrast, calcination of the MOF under nitrogen only produces a mixture of iron(II,III) and iron(III) oxides.

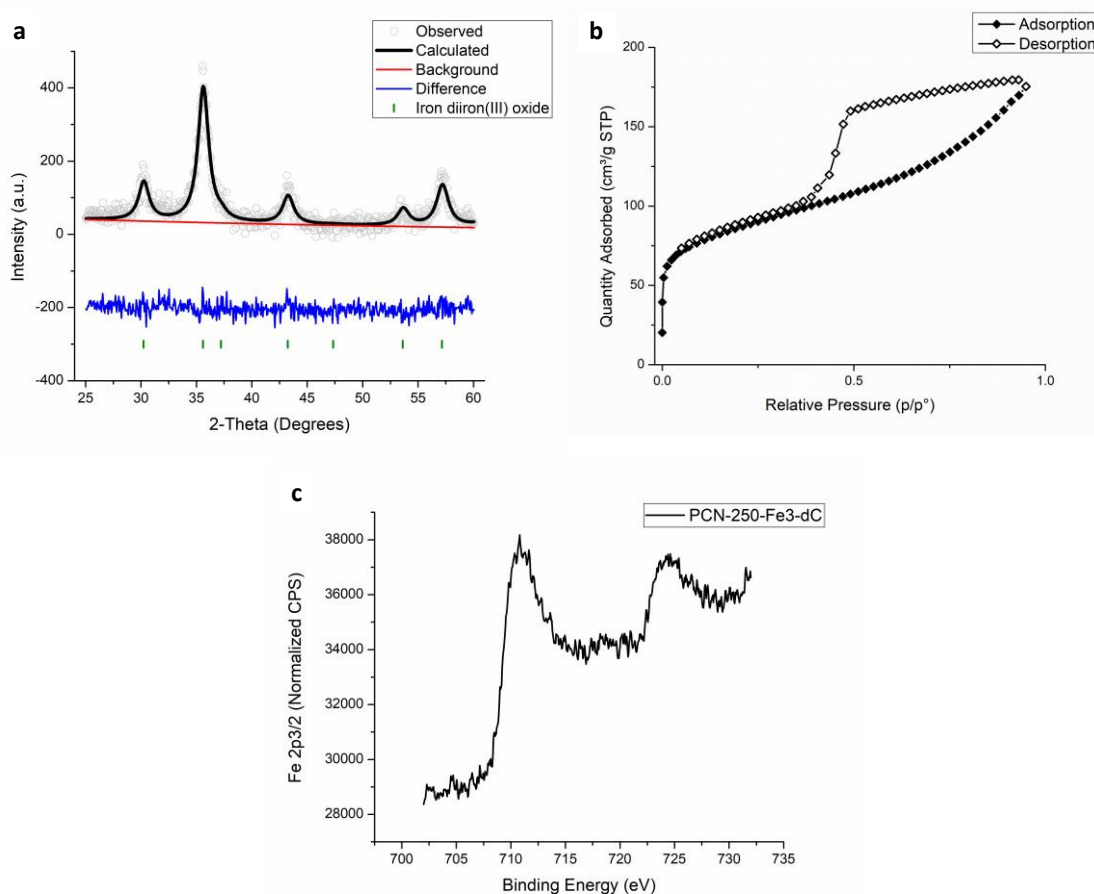


Figure 1. a) Rietveld refinement of PXRD pattern for PCN-250-Fe₃-dC showing only iron(II,III) oxide (magnetite), wR = 6.6%; b) Nitrogen adsorption isotherm of PCN-250-Fe₃-dC collected at 77 K (surface area = 307 m²/g, pore volume = 179.6 cm³/g); c) Fe 2p_{3/2} XPS of PCN-250-Fe₃-dC showing a mixture of iron(II) and iron(III).

Gas sorption analysis reveals a high BET surface area of 307 m²/g in the final MOF_dC. The notable hysteresis of the Type II isotherm indicates significant mesoporosity, as is common for MOF_dCs (Figure 1b). Surprisingly the surface area is even higher than the Brunauer-Emmett-Teller (BET) surface areas of MOF_dCs prepared in single step nitrogen calcinations.¹⁰ We ascribe this to the oxidation of the iron(0)

occurring in an oxygen-free gas environment, which limits combustion of the carbon from the heat generated from the exothermic oxidation.

PCN-250-Fe₂M (M = Mn, Co, Ni)

We then considered the generalizability of the two-step calcination procedure by calcining multimetallic PCN-250, wherein one of the three iron ions in the cluster of the MOF is replaced with a heterometal.^{17, 18} For all three heterometals (M = Mn, Co, Ni), inductively coupled plasma (ICP) confirmed that the metal ratios were similar both before and after calcination, indicating that minimal metal was lost through evaporation (Table 1).

Table 1. Iron/heterometal ratios of multimetallic PCN-250 and PCN-250-dC determined by ICP.

| MOF/MOFdC | MOF Fe:M Ratio | MOFdC Fe:M Ratio |
|----------------------------|-----------------------|-------------------------|
| PCN-250-Fe ₂ Mn | 72:28 | 66:34 |
| PCN-250-Fe ₂ Co | 75:25 | 78:22 |
| PCN-250-Fe ₂ Ni | 66:34 | 61:39 |

We first considered the structure of the metal species derived from the multimetallic MOFs. Rietveld analysis of the PXRD patterns of the heterometallic MOFdCs revealed good incorporation of manganese and cobalt into the iron(II,III) oxide lattice, as no heterometal or heterometal oxide could be identified (Figure 2a-b, Table 2). A small reduction in the lattice parameters of the iron(II,III) oxide unit cell is observed for the cobalt-containing MOFdC, which was expected due to the smaller ionic radius of cobalt compared to iron. Likewise, a slight expansion of the iron(II,III) oxide unit cell was

observed for the manganese-containing MOF_dC, further supporting the conclusion that manganese is incorporated into the iron(II,III) oxide lattice, as manganese has a larger ionic radius than iron. As with the monometallic MOF_dC, both MOF_dCs exhibited small iron(II,III) oxide domain sizes. Fe 2p_{3/2} XPS of each MOF_dC did not reveal any significant shifts in the binding energy of the iron, suggesting that there is monometallic iron(II,III) oxide on the surface of the metal oxide nanoparticles (Figure 3a). This is consistent with the ICP results, which show an overcount of iron compared to the heterometal, indicating that the substitution of the heterometal into the M²⁺ site of the iron(II,III) oxide structure is substoichiometric.

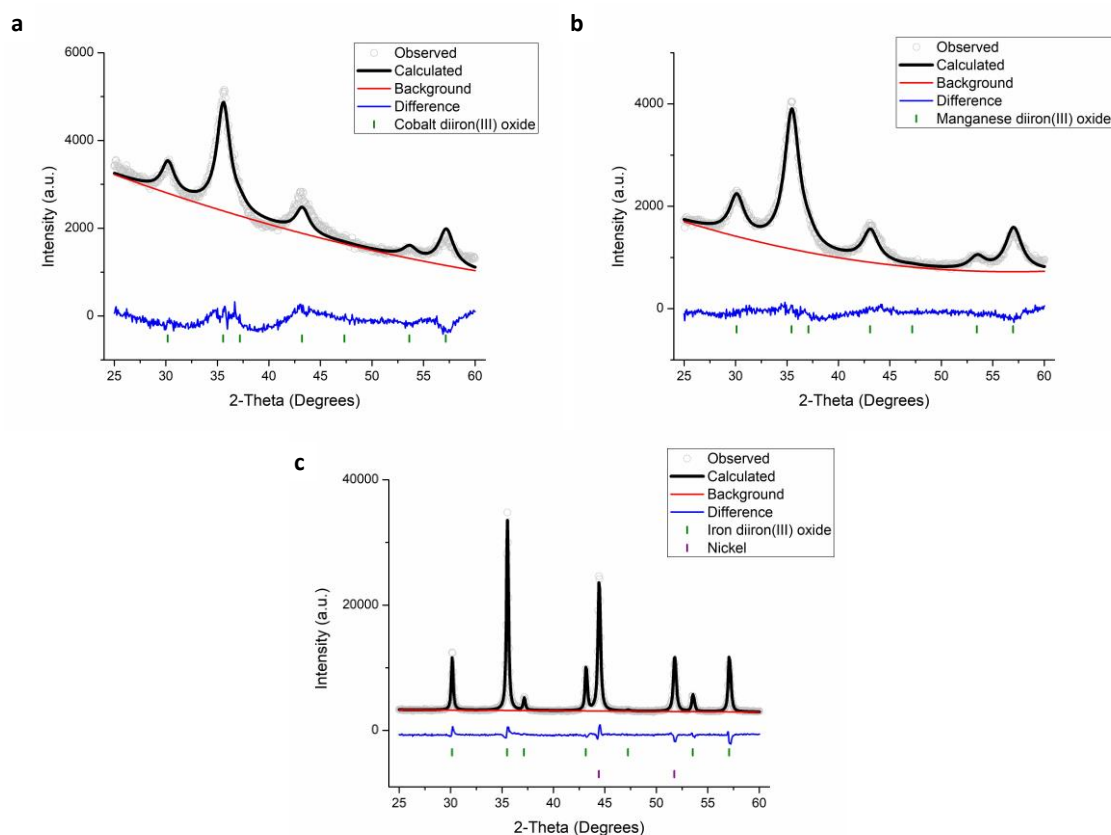


Figure 2. a) Rietveld refinement of PXRD pattern for PCN-250-Fe₂Co-dC showing only cobalt diiron(III) oxide, wR = 5.6%; b) Rietveld refinement of PXRD pattern for PCN-250-Fe₂Mn-dC

showing only manganese diiron(III) oxide, $wR = 4.5\%$; c) Rietveld refinement of PXRD pattern for PCN-250-Fe₂Ni-dC containing a mixture of iron(II,III) oxide and nickel metal and exhibiting sharp Bragg peaks, $wR = 4.0\%$.

Table 2. Rietveld refinement results for multimetallic PCN-250-derived carbons synthesized using the two-step calcination procedure.

| Heterometal | Fe ₂ MO ₄ Phase Fraction | Fe ₂ MO ₄ Domain Size | Heterometal Phase Fraction | Heterometal Phase Domain Size |
|-------------|--|--|----------------------------------|-------------------------------------|
| Mn | 100% | 5.4 nm | - | - |
| Co | 100% | 6.1 nm | - | - |
| Ni | 19% | 55.6 nm | Ni-fcc 81% | 44.9 nm |

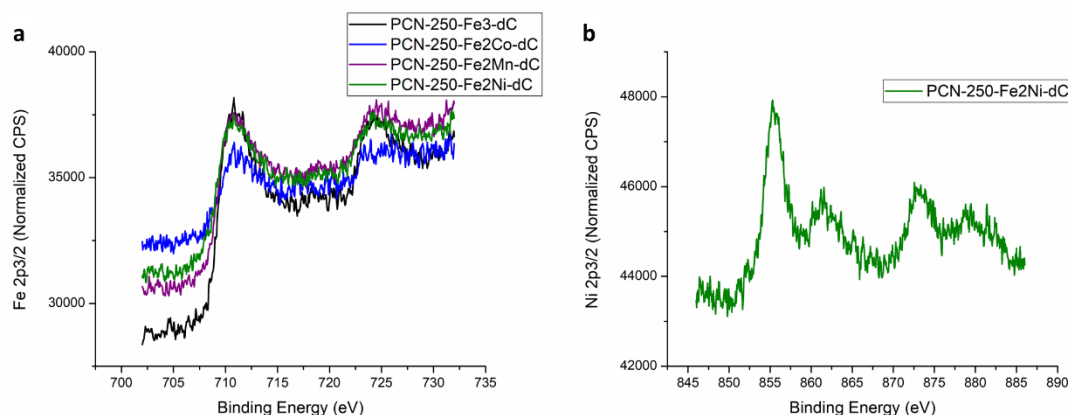


Figure 3. a) Fe 2p_{3/2} XPS spectra of multimetallic MOFDCs showing a mixture of iron(II) and iron(III) oxide; b) Ni 2p_{3/2} XPS of PCN-250-Fe₂Ni-dC resembling the XPS of nickel diiron(III) oxide.

In contrast, the nickel ions were not well-incorporated into the iron(II,III) oxide lattice, as distinct nickel metal peaks were easily identifiable in the powder pattern of the nickel-containing MOFDC (Figure 2c). The results of the Rietveld refinement also suggest an overcount of the nickel phase compared to the amount predicted by the metal ratios observed in the MOF and MOFDC. This suggests that rather than the nickel ions

being incorporated into the iron oxide lattice, iron ions were instead being incorporated into the nickel lattice to form an iron-nickel alloy, which is consistent with the literature.²⁸ Furthermore, there was no discernable change in the lattice parameters of the iron(II,III) oxide phase, which also suggests that the nickel is not incorporated. Surprisingly, there is also no change in the Fe 2p_{3/2} XPS of this MOF_dC, suggesting that there is no significant iron metal on the surface of the nanoparticles (Figure 3a). Furthermore, the Ni 2p_{3/2} XPS shows a spectrum closely matching that of nickel diiron oxide (Figure 3b).³⁰ Given the unambiguous PXRD results, it is hypothesized that a core-shell structure has been formed wherein the surface is comprised of iron(II,III) oxide with a small amount of nickel incorporated in the lattice surrounding a metallic nickel or iron-nickel alloy core. Additionally, the average domain size of the iron(II,III) oxide phase in this MOF_dC was five to ten times those observed for the monometallic, cobalt-containing, and manganese-containing MOF_dCs. We ascribe this increase in domain size to the slower sintering process of iron when alloyed with nickel, which produces fewer defects and larger domains, and stabilization of the γ -Fe phase by the alloyed nickel.³¹

We then considered the porosity of the multimetallic MOF_dCs prepared using the two-step procedure. All three multimetallic MOF_dCs consistently had lower porosities than the monometallic MOF_dC, but all exhibited Type II adsorption isotherms similar to that observed for the monometallic MOF_dC (Figure 4, Table 3). However, there were notable differences in the hysteresis of the desorption curve between the MOF_dCs. The cobalt-containing MOF_dC had the highest BET surface area (214 m²/g) and exhibited a

similar desorption curve to the monometallic MOF_dC, suggesting significant mesoporosity. The lower porosity in this MOF_dC compared to the monometallic MOF_dC is largely a consequence of lower porosity in the template MOF (Figure S3, Table S1). The manganese-containing MOF_dC also had a similar desorption curve, however the step in the curve was notably less, indicating lower mesoporosity. The surface area of this MOF_dC was also smaller (118 m²/g). Both of these observations are likely due to premature framework collapse, as the manganese containing MOF undergoes thermal decarboxylation at a markedly lower temperature (160 °C) than its monometallic, cobalt-, and nickel-containing counterparts (208-220 °C), thus leading to the destruction of the framework pore structure earlier in the calcination process.²⁷ In contrast, the nickel-containing MOF_dC did not show significant hysteresis, indicating that the structure exhibited significantly lower mesoporosity, and had the lowest BET surface area (104 m²/g), despite the template MOF exhibiting a high surface area. This is ascribed to the larger metal and metal oxide particles occupying pore space. The magnitude of the differences in surface area makes it unlikely that the differences are primarily due to the different densities of the respective metal species given that the densities of the mixed metal oxides are within 5% of that of the heterometallic oxide.³²⁻³⁴

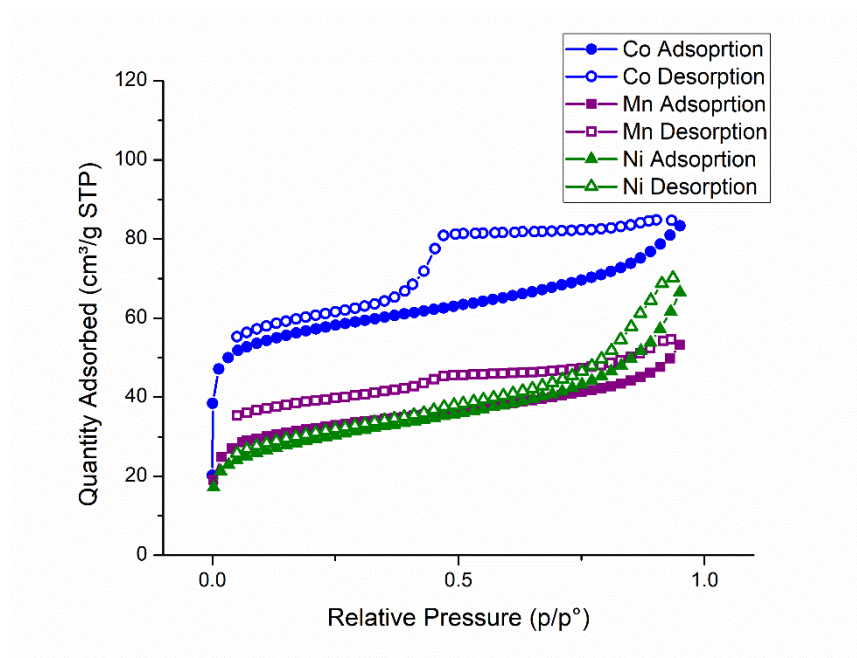


Figure 4. Nitrogen adsorption isotherms of multimetallic MOFDCs synthesized using the two-step calcination procedure.

Table 3. BET surface areas and pore volumes of multimetallic MOFDCs.

| MOFDC | BET Surface Area (m ² /g) | Pore Volume (cm ³ /g) |
|-------------------------------|--------------------------------------|----------------------------------|
| PCN-250-Fe ₂ Co-dC | 214 | 84.8 |
| PCN-250-Fe ₂ Mn-dC | 118 | 54.6 |
| PCN-250-Fe ₂ Ni-dC | 104 | 70.1 |

To determine the underlying cause of the different behavior of the nickel-containing MOF, we considered the phases produced by calcination in nitrogen only. While a previous study has observed no iron(0) in the final material when the MOF is calcined in nitrogen only,¹⁰ we found that some body-centered cubic (bcc) α -Fe phase of iron(0) remained in addition to iron(III) and iron(II,III) oxides, even after exposure to ambient air (Figure 5a). The PXRD of both the cobalt- and manganese-containing

MOF_dCs also exhibited peaks corresponding to bcc α -Fe, possibly alloyed with the heterometal (Figure 5b-c). This is not unexpected, as the bcc structure is the most common reported structure for both cobalt and manganese alloys of iron according to a survey of the Inorganic Crystal Structure Database (ICSD).^{35, 36} The manganese-containing MOF_dC also exhibited peaks corresponding to manganese(III) iron(III) oxide, similar to the iron(III) oxide peaks observed in the monometallic MOF_dC.

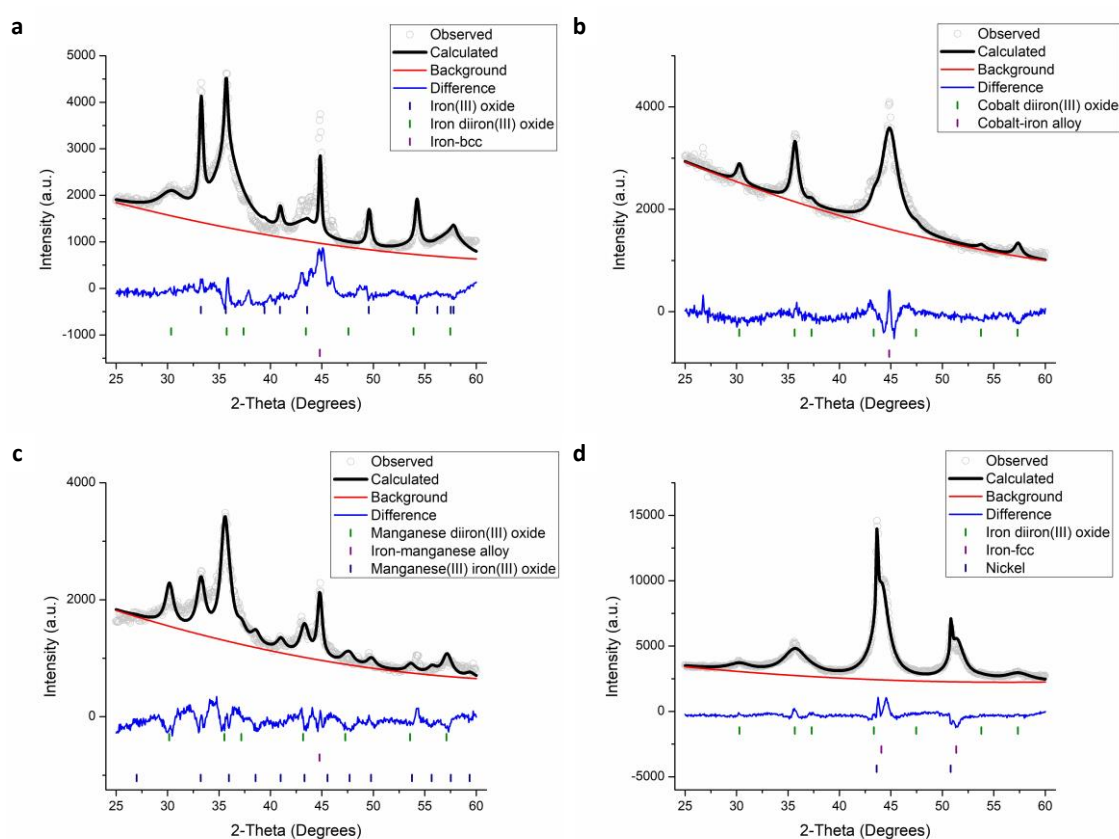


Figure 5. Rietveld refinements of PXRD patterns for a) PCN-250-Fe₃-dC produced using the single-step calcination procedure showing a mixture of iron(III) oxide, iron(II,III) oxide, and bcc iron(0), wR = 10.5%; b) PCN-250-Fe₂Co-dC produced using the single-step calcination procedure showing a mixture of cobalt diiron(III) oxide, and bcc iron-cobalt alloy, wR = 4.5%; c) PCN-250-Fe₂Mn-dC produced using the single-step calcination procedure showing a mixture of manganese iron(III) oxide, manganese diiron(III) oxide, and bcc iron-manganese alloy, wR = 7.1%; d) PCN-250-Fe₂Ni-dC produced using the single-step calcination procedure showing a mixture of iron(II,III) oxide, fcc nickel(0) and fcc iron(0) wR = 4.8%.

In contrast, the PXRD of the nickel-containing MOF_dC exhibited peaks corresponding to the face-centered cubic (fcc) γ -Fe phase of iron (Figure 5d), which is significantly more common than the bcc structure for FeNi alloys according to a survey of the ICSD.^{35, 36} The PXRD of the nickel-containing MOF exhibited sharp peaks in this region closely followed by a broader shoulder, which have been modeled as distinct iron and nickel phases, suggesting some degree of phase separation of the two metals under these conditions. This suggests that the underlying cause of the differences with the nickel-containing MOF_dC is the relative stability of the iron-nickel alloy and its high resistance towards corrosion compared to the iron-cobalt and iron-manganese alloys.^{37, 38} The iron-heterometal alloy is formed during the nitrogen calcination step, wherein the iron-heterometal clusters are reduced by the oxidative decomposition of the linkers.^{10, 26, 27} In the case of nickel, the alloy is sufficiently resistant to corrosion during the carbon dioxide calcination step, as evidenced by the greater fraction of metallic species present in the final material. This corrosion-resistance is similarly observed when the nickel-containing MOF is calcined under nitrogen only, as limited oxidation occurs upon exposure to air at ambient temperature. In contrast, the incorporation of manganese and cobalt does not significantly increase the corrosion-resistance of the iron species under the carbon dioxide atmosphere, thus resulting in an iron(II,III) oxide structure as the metals are oxidized by the carbon dioxide at high temperature. These results demonstrate that the two-step calcination procedure is not entirely generalizable

but can be applied for multimetallic PCN-250 where the heterometal does not significantly enhance the corrosion resistance of the iron when alloyed.

Conclusions

By exploiting the established decomposition mechanisms of PCN-250, we have developed a calcination procedure to maximize both the porosity of the MOF_dC and the fraction of iron(II,III) oxide. Additionally, we have demonstrated that the two-step calcination procedure is generalizable for the production of bimetallic iron-heterometal(II,III) oxides derived from bimetallic PCN-250-Fe₂M (M = Mn, Co). However, the procedure cannot produce a significant fraction of iron-nickel(II,III) oxide due to the corrosion resistance of the iron-nickel alloy that is produced after the nitrogen step of the calcination. Studies on the electrochemical properties of the multimetallic MOF_dCs are ongoing.

Acknowledgements

This work was supported by the Welch Foundation through the Welch Endowed Chair to H.C.Z. A-0030. The use of the Texas A&M X-ray Diffraction Laboratory is acknowledged. The X-ray diffractometers and crystallographic computing systems were purchased with funds provided by the National Science Foundation (CHE-9807975, CHE-0079822, and CHE-0215838). The authors acknowledge the Texas A&M Materials Characterization Facility for assistance with XPS experiments. The authors

would also like to thank Professor Sarbajit Banerjee for the provision of equipment and *framergy*, Inc. for their support.

Notes

J.A.P, D.E.Y., and H.-C.Z. declare the following competing financial interest(s): The authors declare a financial interest in *framergy*, Inc., a startup company that is commercializing the MOFs studied in this paper.

References

1. Frameworks for commercial success. *Nat. Chem.* **2016**, 8 (11), 987-987.
2. Ding, M.; Cai, X.; Jiang, H.-L., Improving MOF stability: approaches and applications. *Chem. Sci.* **2019**, 10 (44), 10209-10230.
3. Mouchaham, G.; Wang, S.; Serre, C., The stability of metal–organic frameworks. In *Metal-Organic Frameworks: Applications in Separations and Catalysis*, Garcia, H.; Navalon, S., Eds. Wiley-VCH: Weinheim, 2018; pp 1-28.
4. Liu, B.; Shioyama, H.; Akita, T.; Xu, Q., Metal-Organic Framework as a Template for Porous Carbon Synthesis. *J. Am. Chem. Soc.* **2008**, 130 (16), 5390-5391.
5. Chaikittisilp, W.; Ariga, K.; Yamauchi, Y., A new family of carbon materials: synthesis of MOF-derived nanoporous carbons and their promising applications. *J. Mater. Chem. A* **2013**, 1 (1), 14-19.

6. Oar-Arteta, L.; Wezendonk, T.; Sun, X.; Kapteijn, F.; Gascon, J., Metal organic frameworks as precursors for the manufacture of advanced catalytic materials. *Mater. Chem. Front.* **2017**, *1* (9), 1709-1745.
7. Jiang, H.-L.; Liu, B.; Lan, Y.-Q.; Kuratani, K.; Akita, T.; Shioyama, H.; Zong, F.; Xu, Q., From Metal–Organic Framework to Nanoporous Carbon: Toward a Very High Surface Area and Hydrogen Uptake. *J. Am. Chem. Soc.* **2011**, *133* (31), 11854-11857.
8. Yin, P.; Yao, T.; Wu, Y.; Zheng, L.; Lin, Y.; Liu, W.; Ju, H.; Zhu, J.; Hong, X.; Deng, Z.; Zhou, G.; Wei, S.; Li, Y., Single Cobalt Atoms with Precise N-Coordination as Superior Oxygen Reduction Reaction Catalysts. *Angew. Chem. Int. Ed.* **2016**, *55* (36), 10800-10805.
9. Day, G. S.; Drake, H. F.; Contreras-Ramirez, A.; Ryder, M. R.; Page, K.; Zhou, H.-C., Controlled Metal Oxide and Porous Carbon Templation Using Metal-Organic Frameworks. *Cryst. Growth Des.* **2021**, *21* (8), 4249-4258.
10. Day, G. S.; Li, J.; Joseph, E. A.; Metz, P.; Perry, Z.; Ryder, M. R.; Page, K.; Zhou, H.-C., Metal oxide decorated porous carbons from controlled calcination of a metal-organic framework. *Nanoscale Adv.* **2020**, *2* (7), 2758-2767.
11. Wang, H.; Wang, Y.; Li, Y.; Lan, X.; Ali, B.; Wang, T., Highly Efficient Hydrogenation of Nitroarenes by N-Doped Carbon-Supported Cobalt Single-Atom Catalyst in Ethanol/Water Mixed Solvent. *ACS Appl. Mater. Interfaces* **2020**, *12* (30), 34021-34031.

12. Shankar, A.; Maduraiveeran, G., Bimetallic iron cobalt oxide nanoclusters embedded on three-dimensional flower-like iron cobalt oxide nanosheets for improved oxygen evolution reaction. *Energy Adv.* **2022**, *1* (8), 562-571.
13. Sayeed, M. A.; O'Mullane, A. P., Electrodeposition at Highly Negative Potentials of an Iron-Cobalt Oxide Catalyst for Use in Electrochemical Water Splitting. *ChemPhysChem* **2019**, *20* (22), 3112-3119.
14. Otun, K. O.; Liu, X.; Hildebrandt, D., Metal-organic framework (MOF)-derived catalysts for Fischer-Tropsch synthesis: Recent progress and future perspectives. *J. Energy Chem.* **2020**, *51*, 230-245.
15. Fu, A.; Liu, Z.; Sun, Z., Cu/Fe oxide integrated on graphite felt for degradation of sulfamethoxazole in the heterogeneous electro-Fenton process under near-neutral conditions. *Chemosphere* **2022**, *297*, 134257.
16. He, H.; Zhong, Y.; Liang, X.; Tan, W.; Zhu, J.; Yan Wang, C., Natural Magnetite: an efficient catalyst for the degradation of organic contaminant. *Sci. Rep.* **2015**, *5* (1), 10139.
17. Kirchon, A.; Zhang, P.; Li, J.; Joseph, E. A.; Chen, W.; Zhou, H.-C., Effect of Isomorphic Metal Substitution on the Fenton and Photo-Fenton Degradation of Methylene Blue Using Fe-Based Metal–Organic Frameworks. *ACS Appl. Mater. Interfaces* **2020**, *12* (8), 9292-9299.
18. Dong, C.; Yang, J.-J.; Xie, L.-H.; Cui, G.; Fang, W.-H.; Li, J.-R., Catalytic ozone decomposition and adsorptive VOCs removal in bimetallic metal-organic frameworks. *Nat. Commun.* **2022**, *13* (1), 4991.

19. Giménez-Marqués, M.; Santiago-Portillo, A.; Navalón, S.; Álvaro, M.; Briois, V.; Nouar, F.; Garcia, H.; Serre, C., Exploring the catalytic performance of a series of bimetallic MIL-100(Fe, Ni) MOFs. *J. Mater. Chem. A* **2019**, 7 (35), 20285-20292.
20. Hall, J. N.; Bollini, P., Spectroscopic and reactive characterization of mixed-metal Fe–Cr trimer nodes in metal–organic framework MIL-100. *Chem. Commun.* **2023**, 59 (32), 4758-4761.
21. Payra, S.; Devaraj, N.; Tarafder, K.; Roy, S., Unprecedented Electroreduction of CO₂ over Metal Organic Framework-Derived Intermetallic Nano-Alloy Cu_{0.85}Ni_{0.15}/C. *ACS Appl. Energy Mater.* **2022**, 5 (4), 4945-4955.
22. Zhang, Q.; Zhang, X.; Lei, D.; Qiao, S.; Wang, Q.; Shi, X.; Huang, C.; He, G.; Zhang, F., MOF-Derived Hollow Carbon Supported Nickel-Cobalt Alloy Catalysts Driving Fast Polysulfide Conversion for Lithium-Sulfur Batteries. *ACS Appl. Mater. Interfaces* **2023**, 15 (12), 15377-15386.
23. Zheng, F.; Zhu, D.; Shi, X.; Chen, Q., Metal–organic framework-derived porous Mn_{1.8}Fe_{1.2}O₄ nanocubes with an interconnected channel structure as high-performance anodes for lithium ion batteries. *J. Mater. Chem. A* **2015**, 3 (6), 2815-2824.
24. Guo, H.; Li, T.; Chen, W.; Liu, L.; Yang, X.; Wang, Y.; Guo, Y., General design of hollow porous CoFe₂O₄ nanocubes from metal–organic frameworks with extraordinary lithium storage. *Nanoscale* **2014**, 6 (24), 15168-15174.
25. Castells-Gil, J.; Ould-Chikh, S.; Ramírez, A.; Ahmad, R.; Prieto, G.; Gómez, A. R.; Garzón-Tovar, L.; Telalovic, S.; Liu, L.; Genovese, A.; Padial, N. M.; Aguilar-Tapia, A.; Bordet, P.; Cavallo, L.; Martí-Gastaldo, C.; Gascon, J., Unlocking

- mixed oxides with unprecedented stoichiometries from heterometallic metal-organic frameworks for the catalytic hydrogenation of CO₂. *Chem Catal.* **2021**, *1* (2), 364-382.
26. Drake, H. F.; Day, G. S.; Vali, S. W.; Xiao, Z.; Banerjee, S.; Li, J.; Joseph, E. A.; Kuszynski, J. E.; Perry, Z. T.; Kirchon, A.; Ozdemir, O. K.; Lindahl, P. A.; Zhou, H.-C., The thermally induced decarboxylation mechanism of a mixed-oxidation state carboxylate-based iron metal–organic framework. *Chem. Commun.* **2019**, *55* (85), 12769-12772.
27. Drake, H. F.; Xiao, Z.; Day, G. S.; Vali, S. W.; Chen, W.; Wang, Q.; Huang, Y.; Yan, T.-H.; Kuszynski, J. E.; Lindahl, P. A.; Ryder, M. R.; Zhou, H.-C., Thermal decarboxylation for the generation of hierarchical porosity in isostructural metal–organic frameworks containing open metal sites. *Mater. Adv.* **2021**, *2* (16), 5487-5493.
28. Chen, Z.; Chen, Z.; Farha, O. K.; Chapman, K. W., Mechanistic Insights into Nanoparticle Formation from Bimetallic Metal–Organic Frameworks. *J. Am. Chem. Soc.* **2021**, *143* (24), 8976–8980.
29. Oleksak, R. P.; Addou, R.; Gwalani, B.; Baltrus, J. P.; Liu, T.; Diulus, J. T.; Devaraj, A.; Herman, G. S.; Doğan, Ö. N., Molecular-scale investigation of the oxidation behavior of chromia-forming alloys in high-temperature CO₂. *npj Mater. Degrad.* **2021**, *5* (1), 46.
30. McIntyre, N. S.; Cook, M. G., X-ray photoelectron studies on some oxides and hydroxides of cobalt, nickel, and copper. *Anal. Chem.* **1975**, *47* (13), 2208-2213.
31. Chan, T.-Y.; Lin, S.-T., Sintering of elemental carbonyl iron and carbonyl nickel powder mixtures. *J. Mater. Sci.* **1997**, *32* (8), 1963-1967.

32. Yunus, S. M.; Yamauchi, H.; Zakaria, A. K. M.; Igawa, N.; Hoshikawa, A.; Ishii, Y., Cation distribution and crystallographic characterization of the quaternary spinel system $\text{Mg}_x\text{Co}_{1-x}\text{Cr}_x\text{Fe}_{2-x}\text{O}_4$. *J. Alloys Compd.* **2008**, *454* (1), 10-15.
33. Wende, C.; Olimov, K.; Modrow, H.; Wagner, F. E.; Langbein, H., Cation distribution, structure and magnetic properties of lithium manganese iron oxide spinel solid solutions. *Mater. Res. Bull.* **2006**, *41* (8), 1530-1542.
34. Fleet, M., The structure of magnetite. *Acta Crystallogr. Sect. B* **1981**, *37* (4), 917-920.
35. Inorganic Crystal Structure Database. FIZ Karlsruhe: 2023.
36. Zagorac, D.; Müller, H.; Ruehl, S.; Zagorac, J.; Rehme, S., Recent developments in the Inorganic Crystal Structure Database: theoretical crystal structure data and related features. *J. Appl. Crystallogr.* **2019**, *52* (5), 918-925.
37. Harner, L. L., Invar at 100 years. *Adv. Mater. Process.* **1997**, *151* (5), 31-35.
38. Adull Manan, N. F.; Nik Mohd Masdek, N. R.; Abdul Aziz, Q.; Salleh, Z., The study of corrosion behaviour of Cobalt-Iron (CoFe) alloy coating. *J. Mech. Eng.* **2017**, (4), 167-183.